Received: 5 October 2023 | Revised: 24 May 2024 | Accepted: 31 May 2024

DOI: 10.1002/cnm.3839

BASIC RESEARCH

WILEY

Analysis of the effect of inert gas on alveolar/venous blood partial pressure by using the operator splitting method

Jyoti[1] | **Soobin Kwak**[2] | **Seokjun Ham**[2] | **Youngjin Hwang**[2] | **Seungyoon Kang**[2] | **Junseok Kim**[2]

[1]The Institute of Basic Science, Korea University, Seoul, Republic of Korea

[2]Department of Mathematics, Korea University, Seoul, Republic of Korea

Correspondence
Junseok Kim, Department of Mathematics, Korea University, Seoul 02841, Republic of Korea.
Email: cfdkim@korea.ac.kr

Funding information
National Research Foundation of Korea (NRF) funded by the Ministry of Science and ICT, Grant/Award Number: 2022H1D3A2A02081237

Abstract

This study aims to investigate how inert gas affects the partial pressure of alveolar and venous blood using a fast and accurate operator splitting method (OSM). Unlike previous complex methods, such as the finite element method (FEM), OSM effectively separates governing equations into smaller subproblems, facilitating a better understanding of inert gas transport and exchange between blood capillaries and surrounding tissue. The governing equations were discretized with a fully implicit finite difference method (FDM), which enables the use of larger time steps. The model employed partial differential equations, considering convection-diffusion in blood and only diffusion in tissue. The study explores the impact of initial arterial pressure, breathing frequency, blood flow velocity, solubility, and diffusivity on the partial pressure of inert gas in blood and tissue. Additionally, the effects of anesthetic inert gas and oxygen on venous blood partial pressure were analyzed. Simulation results demonstrate that the high solubility and diffusivity of anesthetic inert gas lead to its prolonged presence in blood and tissue, resulting in lower partial pressure in venous blood. These findings enhance our understanding of inert gas interaction with alveolar/venous blood, with potential implications for medical diagnostics and therapies.

KEYWORDS

alveolar/venous blood, diffusion, gas exchange, inert gas, operator splitting method, partial pressure, respiratory system

1 | INTRODUCTION

The term "inert" is used to describe gases with low chemical reactivity. The atmosphere contains naturally occurring inert gases, such as argon (Ar), helium (He), krypton (Kr), neon (Ne), nitrogen (N_2), radon (Rn), and xenon (Xe). These gases' inert nature makes them useful in various applications, such as providing a nonreactive environment for certain chemical reactions, serving as carrier gases in analytical instruments, and being used as protective atmospheres in industrial processes. Nitrogen is the most abundant inert gas. Additionally, helium and argon are commonly used in breathing mixtures for divers. Xenon has anesthetic properties and is used in surgical procedures.

Besides these applications, there may be some health risks due to the imbalance in anesthesia[1–3] and excessive inhalation of certain inert gases, such as radon, atmospheric nitrogen,[4–7] helium,[8–10] and argon. These gases primarily affect

the oxygen level[11–14] in the blood, which causes an imbalance of partial pressure of gases in arterial as well as venous blood.[15] Here, the term partial pressure is defined as the pressure exerted by a particular gas alone.[16,17]

Generally, in the process of respiration, we inhale a mixture of gases, which are exchanged between the air-blood barrier through the process of simple diffusion with the help of the partial pressure of gases.[18] In the context of blood gas analysis, the partial pressure of gases in oxygenated blood (upon entering the body) is referred to as "arterial blood partial pressure," while in deoxygenated blood (as it exits the body), it is termed "venous blood partial pressure."[17]

Due to excess inhalation of inert gas and imbalance in anesthesia, the partial pressure affects the arterial blood as well as the venous blood, which causes impaired gas exchange not only in young people but also in elderly.[14,19–23] In literature, there are various theoretical studies[5,6,8,9,24,25] on the attempt of suicide by inhalation of an excessive amount of inert gas. In a forensic investigation, it was documented that a 37-year-old male was discovered unresponsive inside his vehicle, with five liquid nitrogen tanks found in the trunk,[4] indicating excessive inhalation of nitrogen gas. Additionally, a helium suicide case was also identified in Carfora et al.[8]

Furthermore, in a study by Hedenstierna and Rothen,[26] it was observed that during general anesthesia with mechanical ventilation, there was a consistent impairment in pulmonary gas exchange, resulting in decreased blood oxygenation and potential lung tissue collapse. Another physiological study conducted by Strandberg et al.[3] examined 14 patients who underwent anesthesia, using computerized tomography. The findings revealed that within 5–10 min of anesthesia, all patients developed lung densities in a dependent, crest-shaped pattern. Notably, in nine out of ten patients, these densities persisted 1 h after surgery, and in five out of ten patients, they were still present 24 h after anesthesia. From the literature, we found that inhaling inert gases to a significant extent can result in adverse health effects.[1] Unfortunately, these gases are colorless and odorless, making them difficult to detect using standard toxicological analysis. Additionally, their hidden nature poses an added challenge in identifying their presence. Once inhaled, these gases mix with oxygen in the lungs and are transported through the bloodstream, affecting both the partial pressure of oxygen in the blood and tissues.

In recent years, numerous studies have explored various methodologies for facilitating gas exchange between tissues and capillaries. For instance, Singh et al.[27] investigated the simultaneous transportation of oxygen and carbon dioxide within systemic capillaries and surrounding tissues under hyperbaric conditions, employing the eigenfunction expansion method. Additionally, to calculate the alveolar partial pressure of carbon monoxide Sharan et al.[28] applied the Newton–Raphson method and found that the alveolar partial pressure increased exponentially with time and attained an asymptotic value for a given atmospheric carbon monoxide concentration. Another study by Sharan et al.[29] utilized the finite element method (FEM) to solve the transportation of oxygen in the systemic capillaries and surrounding tissues, however, to resolve the nonlinearities of the system the authors used a fixed-point iterative technique. Melo et al.[30] applied the downhill simplex method and observed that accounting for diffusing capacity and ventilation-perfusion heterogeneity increased oxygen arterial pressure while decreasing total blood flow. Additionally, in the process of inert gas exchange between tissue and blood capillaries, Whiteley et al.[17] used FEM to calculate the mixed-venous blood partial pressure, which is return to the lungs. Furthermore, Baker and Framery[31] used an analytical method to solve the transportation of inert gas between tissue and blood capillaries using a multi compartment model, while to calculate some values in the single compartment model author used some iterative method. In continuation recently, Kori and Pratibha[16] calculated intercapillary gas exchange with the effects of aging and various lung diseases using the explicit finite difference method (FDM).

To solve some physical problems in axisymmetric or simple domains we need an appropriate approach that can be employed efficiently in terms of accuracy and computational cost. One such approach is the operator splitting method (OSM), where the problem is divided into smaller sub-problems and solved level by level. From the literature OSM has found application in advection–diffusion problems. For instance, Ravshanov et al.[32] calculated the transport and diffusion of air pollutants in the atmospheric boundary layer by using OSM together with a second-order implicit finite-difference scheme in time and stated that OSM provides sufficient accuracy of the problem solution compared with field measurement data and it has a certain advantage over other numerical methods, such as FDM and the variable substitution method. Similarly, in addressing advection-dispersion-reaction problems, Valocchi and Malmstead[33] utilized OSM to achieve high-order accuracy in the overall solution. Additionally, Liu et al.[34] conducted a convergence analysis and error estimate for the OSM applied to a reaction–diffusion system with detailed balance.

From these studies, we observed that in the context of gas exchange between tissue-blood capillaries in axisymmetric or simple domains partial pressure was found by various complex methods, such as FEM. Therefore, in this study, we investigate the impact of inert gas on the partial pressure of alveolar and venous blood by employing a fast and

accurate OSM, which effectively separates the governing equations into smaller sub-problems so that the transport and exchange of inert gas between blood capillaries and surrounding tissue cylinder can be understood efficiently. We discretized the governing equations using a fully implicit FDM, which allows us to use sufficiently large-time steps. The use of large time step can lead to fast and efficient computation. To model the problem, we used partial differential equations (PDEs), which consist of convection-diffusion in blood and only diffusion in tissue. The effects of initial arterial pressure, breathing frequency, blood flow velocity, solubility, and diffusivity are found on the partial pressure of inert gas in blood and tissue. Additionally, the effect of anesthetic inert gas and oxygen was analyzed on venous blood partial pressure.

The proposed method uses the OSM with implicit FDM, which allows us to use relatively large time steps. Therefore, on an axisymmetric computational domain, we expect that we can achieve fast numerical simulations for a given final time compared with other numerical methods.

Further study is organized as follows. Section 2 presents the governing equations, and Section 3 proposes the methodology for the numerical solution algorithm. Section 4 presents numerical experiments, and Section 5 presents the conclusion.

2 | GOVERNING EQUATIONS

We used a mathematical model that includes one capillary inside the body section. Suppose that the circulation of blood flow inside the body section is homogeneous. Blood flows inside a thin capillary, which is surrounded by an interstitial space. The tissue can be considered as the interstitial space. Inert gas is passed inside the blood, which will be diffused through blood–tissue interface into the interstitial space. Figure 1 presents the schematic of the physical problem.

To study flux transformation phenomena, we consider the convection-diffusion equation in blood and tissue separately with interface conditions and some initial and boundary conditions as proposed by Whiteley et al.,[17] and others.[29,35,36] In the blood phase, we consider both convection and diffusion, while in the tissue phase, we consider only diffusion. Due to radial symmetry, cylindrical polar coordinates are used to simplify the problem into two spatial dimensions. The governing equations for the partial pressure of inert gas $P(r,z,t)$ in blood and tissue are defined as follows:

$$\alpha_b\left(\frac{\partial P(r,z,t)}{\partial t}+w\frac{\partial P(r,z,t)}{\partial z}\right)=\alpha_b D_b\left[\frac{1}{r}\frac{\partial}{\partial r}\left(r\frac{\partial P(r,z,t)}{\partial r}\right)+\frac{\partial^2 P(r,z,t)}{\partial z^2}\right], \tag{1}$$

$$0<r<R_b,\ 0<z<d,$$

$$\alpha_t\frac{\partial P(r,z,t)}{\partial t}=\alpha_t D_t\left[\frac{1}{r}\frac{\partial}{\partial r}\left(r\frac{\partial P(r,z,t)}{\partial r}\right)+\frac{\partial^2 P(r,z,t)}{\partial z^2}\right], \tag{2}$$

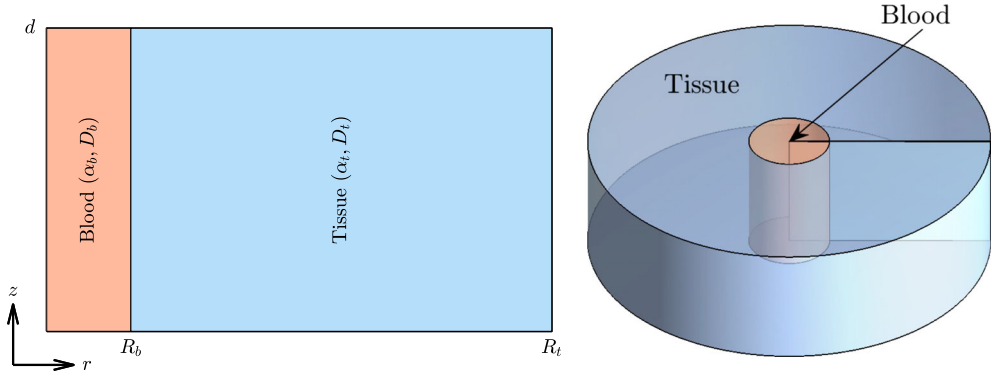

FIGURE 1 Schematic illustration of physical problem.

$$R_b < r < R_t,\ 0 < z < d,$$

where w is a constant velocity, r is radial coordinate, z is axial coordinate, R_b is blood capillary radius, R_t is tissue radius, d is axial length of capillary, D_b is diffusion coefficient in plasma, D_t is diffusion coefficient in tissue, α_b is solubility in plasma, and α_t is solubility in tissue. To solve the governing equation, we use the following initial condition:

$$P(r,z,0) = 0,\ \text{for}\, 0 \le r \le R_t,\ \text{and}\, 0 \le z \le d, \tag{3}$$

and defined the boundary conditions as: Input arterial blood partial pressure P_a is,

$$P(r,0,t) = P_a(r,0,t) = P_0 \exp(-ft),\quad \text{for}\, 0 \le r \le R_b, \tag{4}$$

where P_0 is initial arterial partial pressure difference entering in capillary, and f is frequency of breathing.

Radial symmetry implies that,

$$\frac{\partial P(r,z,t)}{\partial r} = 0,\quad \text{for}\, r = 0,\ 0 \le z \le d. \tag{5}$$

The flux is zero across closed boundaries,

$$\frac{\partial P(r,z,t)}{\partial r} = 0,\quad \text{for}\, r = R_t,\ 0 \le z \le d, \tag{6}$$

$$\frac{\partial P(r,z,t)}{\partial z} = 0,\quad \text{for}\, R_b \le r \le R_t,\ z = 0\ \text{and}\ d, \tag{7}$$

and no diffusion flux is taken at the end of capillary,

$$\frac{\partial P(r,z,t)}{\partial z} = 0,\quad \text{for}\, 0 \le r \le R_b,\ z = d. \tag{8}$$

In addition, $P(r,z,t)$ and flux are continuous across the interface, therefore,

$$P(r,z,t)\Big|_{r=R_b^-} = P(r,z,t)\Big|_{r=R_b^+},\quad \text{for}\, 0 \le z \le d, \tag{9}$$

$$\alpha_b D_b \frac{\partial P(r,z,t)}{\partial r}\Big|_{r=R_b^-} = \alpha_t D_t \frac{\partial P(r,z,t)}{\partial r}\Big|_{r=R_b^+},\quad \text{for}\, 0 \le z \le d. \tag{10}$$

3 | METHODOLOGY

3.1 | Numerical solution algorithm

To solve the governing equation with boundary conditions, we employ the OSM. Figure 2 demonstrates the computational grid, which consists of rectangular cells of size Δr by Δz. These cells Ω_{ik} are centered in r-direction with $r_i = (i-.5)\Delta r$, where $i = 1,2,3,...,b-1,b,b+1,...,N_r$ with $\Delta r = R_b/(b-.5)$, $N_r = 10b-5$ so that we can get $r_{N_r} + \Delta r/2 = R_t$ and in z-direction with $z_k = (k-.5)\Delta z$ for $k = 1,2,...,N_z$. Here, N_r and N_z are number of cells in r- and z-directions, respectively. The grid point r_b is at the interface (blood–tissue barrier) through which flux will be continuously diffused from the blood phase (from grid point r_{b-1}) to the tissue phase (to grid point r_{b+1}). Three different color symbols (•, ◆, ◆) are used to show the interface and ghost points as well as respective boundary conditions. Let P_{ik}^n be

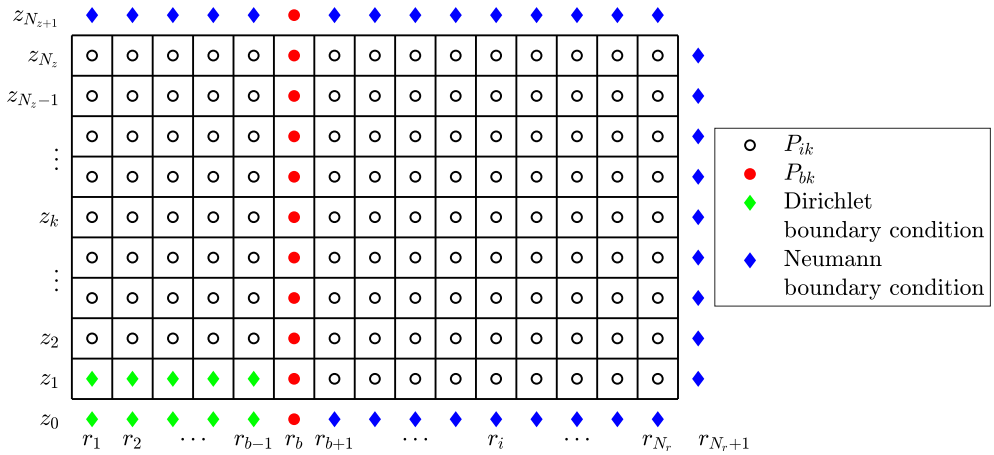

FIGURE 2 Schematic illustration of computational grid.

the numerical approximation of $P(r_i,z_k,t_n)$ where $t_n = n\Delta t$ and Δt is a time step. The discrete partial pressure field P^c_{ik} for $c = n, n+\frac{1}{2}, n+1$ and the pressure at the interface $P^{n+\frac{1}{2}}_{bk}$ are located at cell centers.

3.2 | Algorithm

We applied OSM in Equations (1) and (2). Then, both the equations are splitted into two equations. First one is a PDE in r-direction and second one is a PDE in z-direction. Therefore, we have equations in r- and z-directions as,

r-direction equation:

$$\frac{\partial P(r,z,t)}{\partial t} = \begin{cases} \frac{D_b}{r}\frac{\partial}{\partial r}\left(r\frac{\partial P(r,z,t)}{\partial r}\right) & \text{for } 0 < r < R_b, \\ \frac{D_t}{r}\frac{\partial}{\partial r}\left(r\frac{\partial P(r,z,t)}{\partial r}\right) & \text{for } R_b < r < R_t, \end{cases} \tag{11}$$

$$P\left(R_b^-,z,t\right) = P\left(R_b^+,z,t\right) \qquad \text{on interface,} \tag{12}$$

$$\alpha_b D_b \frac{\partial P(r,z,t)}{\partial r}\bigg|_{r=R_b^-} = \alpha_t D_t \frac{\partial P(r,z,t)}{\partial r}\bigg|_{r=R_b^+} \qquad \text{on interface.} \tag{13}$$

z-direction equation:

$$\frac{\partial P(r,z,t)}{\partial t} = \begin{cases} D_b \frac{\partial^2 P(r,z,t)}{\partial z^2} - w\frac{\partial P(r,z,t)}{\partial z} & \text{for } 0 < r < R_b, \\ D_t \frac{\partial^2 P(r,z,t)}{\partial z^2} & \text{for } R_b < r < R_t. \end{cases} \tag{14}$$

On a given time $n\Delta t$, P^n_{ik} is the initial condition of the r-direction equations, and the solution of the r-direction equation is the initial condition of the z-direction equations. Using a FDM,[37] we will discretize the split equations on the numerical grid as defined in Appendix A with the notation given at Section 3.1.

- Step 1: Discretization in r-direction,

We got following matrices forms,

$$A_1\mathbf{P}_1^{n+\frac{1}{2}} = \mathbf{P}_1^n,$$

where A_1 is an $(N_r-b+1)\times(N_r-b+1)$ matrix,

$$A_1 = \begin{pmatrix} 1+\frac{\alpha_t D_t}{\alpha_b D_b} & -\alpha_t D_t & 0 & \cdots & 0 & 0 & 0 \\ -\alpha_1\left(1-\frac{\Delta r}{2r_{b+1}}\right) & (1+2\alpha_1) & -\alpha_1\left(1+\frac{\Delta r}{2r_{b+1}}\right) & 0 & \cdots & 0 & 0 \\ 0 & -\alpha_1\left(1-\frac{\Delta r}{2r_{b+2}}\right) & (1+2\alpha_1) & -\alpha_1\left(1+\frac{\Delta r}{2r_{b+2}}\right) & 0 & \cdots & 0 \\ \vdots & \vdots & \ddots & \ddots & \ddots & \vdots & \vdots \\ 0 & \cdots & 0 & -\alpha_1\left(1-\frac{\Delta r}{2r_{N_r-2}}\right) & (1+2\alpha_1) & -\alpha_1\left(1+\frac{\Delta r}{2r_{N_r-2}}\right) & 0 \\ 0 & 0 & \cdots & 0 & -\alpha_1\left(1-\frac{\Delta r}{2r_{N_r-1}}\right) & (1+2\alpha_1) & -\alpha_1\left(1+\frac{\Delta r}{2r_{N_r-1}}\right) \\ 0 & 0 & 0 & \cdots & 0 & -\alpha_1\left(1-\frac{\Delta r}{2r_i}\right) & 1+\alpha_1\left(1-\frac{\Delta r}{2r_{N_r}}\right) \end{pmatrix},$$

$$\mathbf{P}_1^{n+\frac{1}{2}} = \left(P_{b1}^{n+\frac{1}{2}},\cdots,P_{N_r1}^{n+\frac{1}{2}}\right)^T \text{ and } \mathbf{P}_1^n = \left(P_{b1}^n,\cdots,P_{N_r1}^n\right)^T. \tag{15}$$

$$A_2\mathbf{P}_k^{n+\frac{1}{2}} = \mathbf{P}_k^n,$$

$$A_2 = \begin{pmatrix} 1+\alpha_2\left(1+\frac{\Delta r}{2r_i}\right) & -\alpha_2\left(1+\frac{\Delta r}{2r_i}\right) & 0 & \cdots & 0 & 0 & 0 \\ -\alpha_2\left(1-\frac{\Delta r}{2r_i}\right) & 1+2\alpha_2 & -\alpha_2\left(1+\frac{\Delta r}{2r_i}\right) & 0 & \cdots & 0 & 0 \\ \vdots & \vdots & \ddots & \ddots & \ddots & \vdots & \vdots \\ 0 & -\alpha_b D_b & \alpha_b D_b+\alpha_t D_t & -\alpha_t D_t & \cdots & 0 & 0 \\ 0 & 0 & -\alpha_1\left(1-\frac{\Delta r}{2r_{b+1}}\right) & (1+2\alpha_1) & -\alpha_1\left(1+\frac{\Delta r}{2r_{b+1}}\right) & 0 & 0 \\ \vdots & \vdots & \ddots & \ddots & \ddots & \vdots & \vdots \\ 0 & \cdots & 0 & -\alpha_1\left(1-\frac{\Delta r}{2r_{N_r-2}}\right) & (1+2\alpha_1) & -\alpha_1\left(1+\frac{\Delta r}{2r_{N_r-2}}\right) & 0 \\ 0 & 0 & \cdots & 0 & -\alpha_1\left(1-\frac{\Delta r}{2r_{N_r-1}}\right) & (1+2\alpha_1) & -\alpha_1\left(1+\frac{\Delta r}{2r_{N_r-1}}\right) \\ 0 & 0 & 0 & \cdots & 0 & -\alpha_1\left(1-\frac{\Delta r}{2r_i}\right) & 1+\alpha_1\left(1-\frac{\Delta r}{2r_{N_r}}\right) \end{pmatrix},$$

where A_2 is an $N_r\times N_r$ matrix, and,

$$\mathbf{P}_k^{n+\frac{1}{2}} = \left(P_{1k}^{n+\frac{1}{2}},\cdots,P_{N_rk}^{n+\frac{1}{2}}\right)^T \text{ and } \mathbf{P}_k^n = \left(P_{1k}^n,\cdots,P_{N_rk}^n\right)^T, \text{for } k=2,...,N_z. \tag{16}$$

- Step 2: Discretization in z-direction for $i=1,...,N_r$.

  We got following matrices forms,

$$B_1\mathbf{P}_i^{n+1} = \mathbf{P}_i^{n+\frac{1}{2}},$$

where B_1 is an $N_z \times N_z$ matrix,

$$B_1 = \begin{pmatrix} 1 & 0 & 0 & \cdots & 0 & 0 & 0 \\ 0 & \beta_3 & \gamma_3 & 0 & \cdots & 0 & 0 \\ 0 & \alpha_3 & \beta_3 & \gamma_3 & \cdots & 0 & 0 \\ 0 & 0 & \alpha_3 & \beta_3 & \gamma_3 & \cdots & 0 \\ \vdots & \vdots & \ddots & \ddots & \ddots & \vdots & \vdots \\ 0 & 0 & \cdots & 0 & \alpha_3 & \beta_3 & \gamma_3 \\ 0 & 0 & 0 & \cdots & 0 & \alpha_3 & \beta_3+\gamma_3 \end{pmatrix},$$

and

$$\mathbf{P}_i^{n+1} = \left(P_{i1}^{n+1}, \cdots, P_{iN_z}^{n+1}\right)^T, \text{for } i = 1,2,...,b-1 \text{ and } \mathbf{P}_i^{n+\frac{1}{2}} = \left(P_{i1}^{n+\frac{1}{2}}, \cdots, P_{iN_z}^{n+\frac{1}{2}}\right)^T.$$

$$B_2\mathbf{P}_i^{n+1} = \mathbf{P}_i^{n+\frac{1}{2}},$$

where B_2 is an $N_z \times N_z$ matrix,

$$B_2 = \begin{pmatrix} \alpha_4+\beta_4 & \gamma_4 & 0 & \cdots & 0 & 0 & 0 \\ \alpha_4 & \beta_4 & \gamma_4 & 0 & \cdots & 0 & 0 \\ 0 & \alpha_4 & \beta_4 & \gamma_4 & \cdots & 0 & 0 \\ 0 & 0 & \alpha_4 & \beta_4 & \gamma_4 & \cdots & 0 \\ \vdots & \vdots & \ddots & \ddots & \ddots & \vdots & \vdots \\ 0 & 0 & \cdots & 0 & \alpha_4 & \beta_4 & \gamma_4 \\ 0 & 0 & 0 & \cdots & 0 & \alpha_4 & \beta_4+\gamma_4 \end{pmatrix},$$

and

$$\mathbf{P}_i^{n+1} = \left(P_{i1}^{n+1}, \cdots, P_{iN_z}^{n+1}\right)^T, \text{and } \mathbf{P}_i^{n+\frac{1}{2}} = \left(P_{i1}^{n+\frac{1}{2}}, \cdots, P_{iN_z}^{n+\frac{1}{2}}\right)^T, \tag{17}$$

for $i = b+1, b+2, ..., N_r$.

Finally, venous blood partial pressure (P_v) can be calculated as,

$$P_v(t) = \frac{2}{R_b^2}\int_0^{R_b} P(r,d,t) r\, dr. \tag{18}$$

After that, Equation (18) is solved using simple Riemann sum rule as,

$$P_v^{n+1} = \frac{2}{R_b^2}\left(\sum_{i=1}^{b-1} P_{i,N_z}^n r_i + P_{b,N_z}^n r_b/2\right)\Delta r. \tag{19}$$

4 | NUMERICAL EXPERIMENTS

In this study, we analyze the effect of inert gas on the partial pressure of alveolar and venous blood. For this purpose, we will focus on the anesthetic gas nitrous oxide (N_2O). For numerical computations, we need values of parameters used in the governing equations. Therefore, we will use Table 1 for numerical computations, including both parameter values and units. Units of pressure and time are in millimeter of mercury and seconds, respectively.[29] Hereafter, units will be omitted for clarity.

4.1 | Validation of scheme

In the following Sections 4.1.1 and 4.1.2, we conduct tests that were also performed in a previous study[17] to validate our scheme.

4.1.1 | Comparison between ordinary differential equation and PDEs models

We utilize the solution of the ordinary differential equation (ODE) model defined in Ref. [17,35] (Refer to these papers for a complete description of the ODE model and parameters) as follows,

$$P_v(t) = P_G\left(1 - \exp\left(-\frac{\dot{Q}t}{V_b'}\right)\right), \tag{20}$$

where P_G is a constant, $\dot{Q}$ is the rate of flow of blood through the capillary, V_b' is the effective volume of the body compartment. Together with the solution of the PDE model obtained by the proposed scheme using Equation (19). In both ODE and PDEs models we used the input arterial blood partial pressure $P_a(t) = 1$ as defined in Ref. [17]. Then we compared both results as shown in Figure 3. From the figure, we observed that both curves tend toward an asymptotic value of 1. However, it was noted that the solution derived from the ODE model converges to this limit significantly faster than the PDEs. A similar result is also found in Ref. [17].

The physiological reason for this behavior may be due to the consideration of spatial variations in inert gas (nitrous oxide) partial pressure in PDE models, which illustrate the effects of tissue heterogeneity, as different tissues absorb and release gases at different rates due to variations in blood flow, tissue solubility, and metabolic activity. Additionally, PDE models consider the shape of the body compartment and the density of the capillaries that supply blood to this

TABLE 1 Parameters used in numerical computations.

Parameter	Value	References
R_b	3.25×10^{-4} cm	[29]
R_t	3.25×10^{-3} cm	[29]
w	.03 cm/s	[29]
$\alpha_b(N_2O)$	2.49×10^{-8} mol cm^{-3} (mmHg)$^{-1}$	[38]
$\alpha_t(N_2O)$	2.78×10^{-8} mol cm^{-3} (mmHg)$^{-1}$	[39]
$D_b(N_2O)$	1.6×10^{-4} cm^2/s	[38]
$D_t(N_2O)$	1.2×10^{-5} cm^2/s	[39]
$\alpha_b(O_2)$	1.527×10^{-9} mol cm^{-3} (mmHg)$^{-1}$	[29]
$\alpha_t(O_2)$	1.295×10^{-9} mol cm^{-3} (mmHg)$^{-1}$	[29]
$D_b(O_2)$	1.12×10^{-5} cm^2/s	[29]
$D_t(O_2)$	1.7×10^{-5} cm^2/s	[29]
f	12–20 breaths/min	[40,41]

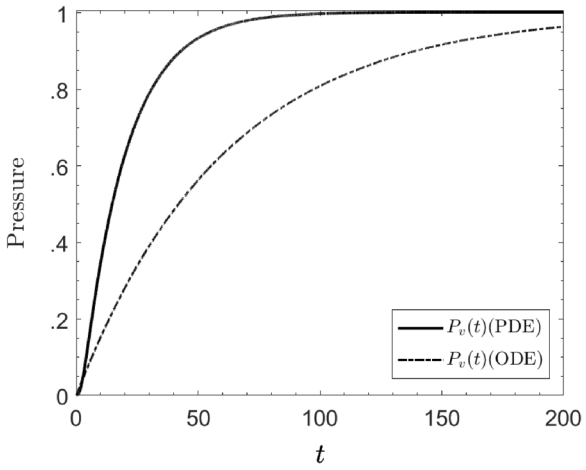

FIGURE 3 $P_v(t)$ calculated using both the PDEs and ODE models depicting the uptake of the anesthetic gas nitrous oxide, with $P_a(t)$ exhibiting a step change from 0 to 1 at time $t = 0$.

tissue. However, ODE models only consider temporal variations, highlighting the impact of gas exchange between tissues and blood over time, including the uptake and elimination of inert gases.

Moreover, to visualize the partial pressure profile inside the blood capillary corresponding to the outflow venous blood partial pressure, we plotted surface diagrams in Figure 4 with a computational domain $\Omega = (0,3.25 \times 10^{-3}) \times (0,162.5 \times 10^{-4})$. We used $N_r = 125$, $N_z = 650$, $\Delta t = .01$, a final time $T = 50$, and an arterial blood partial pressure $P_a(t) = 1$.

4.1.2 | Sinusoidal variations in arterial blood partial pressure

In this subsection, we adopt a sinusoidal form for the partial pressure of gas entering the body compartment, as defined in Ref. [17]: $P_a(t) = P_0 \sin(2\pi f t)$. Next, using the proposed scheme, we generate a combined plot (Figure 5) showing the arterial (P_a) and venous (P_v) blood partial pressures of the gas for both ODE and PDE models over time. Interestingly, our results exhibit a striking similarity to those reported in Ref. [17]. Upon analyzing Figure 5, we observed that when blood enters the body compartment, the arterial partial pressure of the gas is initially quite high. However, it gradually starts to diffuse, and at the outflow boundary, we noted a reduction in the average partial pressure of the gas, whether obtained through ODE or PDE models. Notably, the average partial pressure of the gas in venous blood, as predicted by the ODE model, is significantly lower than that predicted by the PDE model at the outflow boundary. The distinction between ODEs and PDEs lies in the treatment of temporal variation. ODEs only consider temporal variation, whereas PDEs incorporate both temporal variation and the effects of convection and diffusion.

4.2 | Convergence test

To assess the spatial convergence of our numerical solutions using the proposed scheme, we conducted a convergence test as depicted in Figure 6. This figure illustrates the average venous partial pressure along the outflow boundary at time $t = 50$, considering different numbers of grid points N_r and N_z. In the computational domain $\Omega = (0,3.25 \times 10^{-3}) \times (0,162.5 \times 10^{-4})$, we employed a fully implicit scheme, necessitating a sufficiently large time step of $\Delta t = .01$. By analyzing the results presented in Figure 6, we observed that the numerical solutions converge toward the solid line, corresponding to $N_r = 130$ and $N_z = 650$. Consequently, we adopted a grid size of $N_r = 130$ and $N_z = 650$ for all subsequent analyses.

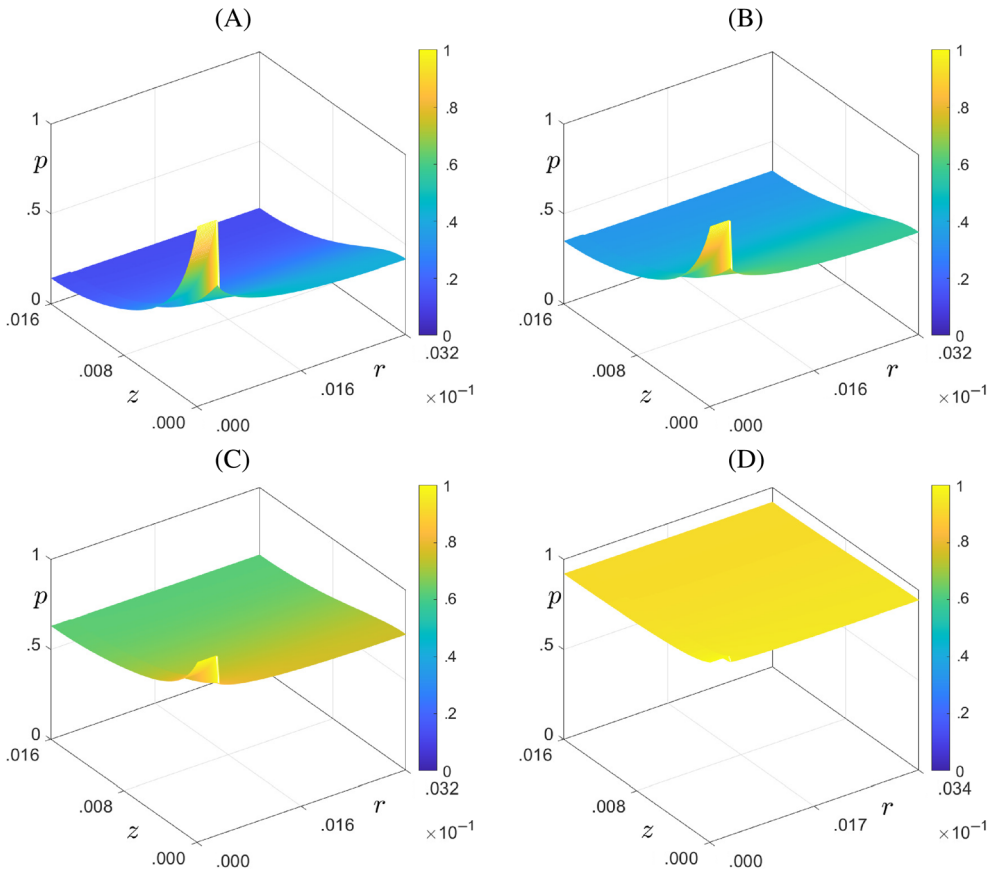

FIGURE 4 Pressure profile corresponding to outflow venous blood partial pressure for different total times (A) $T = 5$, (B) $T = 10$, (C) $T = 20$, and (D) $T = 50$.

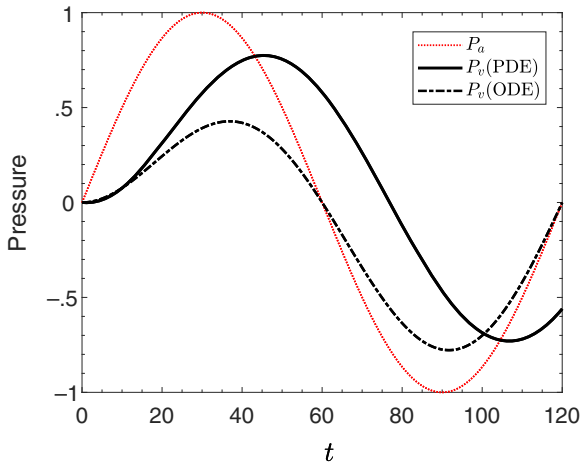

FIGURE 5 A combined plot for input arterial partial pressure $P_a(t)$ and average venous partial pressure (P_v) of gas at outflow boundary using PDE and ODE models for sinusoidal input.

4.3 | Axial effect of breathing frequency on partial pressure of inert gas

The breathing frequency plays a significant role in controlling the levels of inert gases in the blood and tissue capillaries. Changes in breathing frequency can impact alveolar ventilation and arterial partial pressure and, consequently, the removal of inert gases from the lungs.[42,43] Alveolar ventilation, which is the volume of fresh air reaching the alveoli per minute, is a critical factor in controlling the partial pressures of gases in the alveoli. To maintain cardiovascular

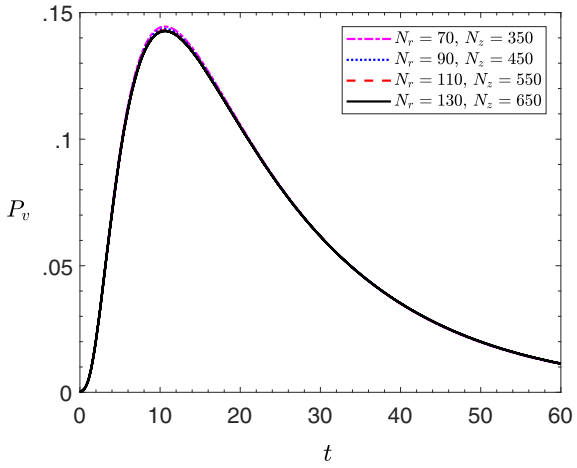

FIGURE 6 Spatial convergence of average venous partial pressure over the outflow boundary for four cases $N_r = 70, N_z = 350$ (dash-dotted line); $N_r = 90, N_z = 450$ (dotted line); $N_r = 110, N_z = 550$ (dashed line); and $N_r = 130, N_z = 650$ (solid line).

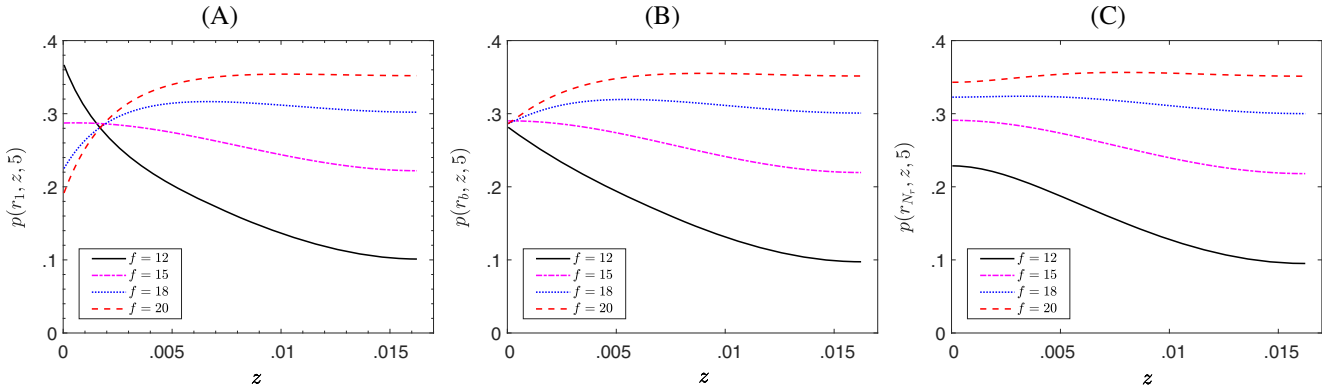

FIGURE 7 Axial effect of breathing frequencies $f = 12,15,18,20$ per minute on (A) center of blood capillary, $p(r_1,z,t)$, (B) boundary of the blood capillary, $p(r_b,z,t)$, and (C) boundary of the tissue $p(r_{N_r},z,t)$ at $t = 5$.

stability and prevent complications, such as changes in blood pressure and heart rate and to optimize gas exchange and intercept hypoxemia (low oxygen levels) or hypercapnia (high carbon dioxide levels) adequate control of breathing frequency is essential because anesthesia can depress the respiratory drive.[44–46]

In this section, we present the effect of breathing frequency on the partial pressure of inert gas. Figure 7 shows the effect of various frequency rates, $f = 12,15,18,20$ per minute, on the center of the blood capillary $p(r_1,z,t)$, axial boundary of the blood $p(r_b,z,t)$ and tissue $p(r_{N_r},z,t)$ capillaries at $t = 5$. We used numerical values as defined in Table 1 at the center of blood capillary $p(r_1,z,t)$. In Figure 7A, initially arterial pressure of inert gas starts from .36 at frequency $f = 12/60$ and tends to decrease with respect to axial length z, after that we increase the breathing frequency $f = 15/60$ and again found a decrement of inert gas partial pressure axially. Then, we choose some high frequencies, such as $f = 18/60, 20/60$ but this time partial pressure of inert gas at the center of the tube, however begins from lower values than previous frequencies but starts to increase with respect to axial distance.

Then we analyze the partial pressure of inert gas at the axial boundary of blood $p(r_b,z,t)$ in Figure 7B and found this time for the lowest frequency partial pressure of inert gas is the lowest while, as we increase frequencies the partial pressure of inert gas will increase accordingly with respect to axial distance. One more noticeable thing is that all the frequencies start at the same point and have the lowest values than the center of the tube. Finally, we analyze the effect of breathing frequency on the axial boundary of tissue in Figure 7C and find that for the lowest frequency the partial pressure of inert gas is lower than the other higher frequencies.

Physiologically, we can say for the lowest frequency rate less amount of inert gas will reach the surrounding tissue of the blood capillary, which will affect less to the patients so the appropriate frequency to take inert gas should be $f \leq 12/60$.

4.4 | Radial effect of breathing frequency on partial pressure of inert gas

In Figure 8 we observe the effect of breathing rates, $f = 12,15,18,20$ per minute, on the entering position of the blood capillary $p(r_i,z_1,t)$, $i = 1,2,...,b$, and its surrounding tissue $p(r_i,z_1,t)$, $i = b+1,b+2,...,N_r$ also on ending position of blood capillary $p\left(r_i,z_{N_z},t\right)$, $i = 1,2,...,b$ and its surround tissue $p\left(r_i,z_{N_z},t\right)$, $i = b+1,b+2,...,N_r$ at $t = 5$. For numerical values, we used Table 1.

In Figure 8A, we found the entering point of the blood capillary for a breathing rate $f = 12$ the partial pressure of inert gas starts approximately at .37 and then becomes constant just before the radial boundary of the blood capillary, after which it slightly declines. Then we increased the breathing rate $f = 15$ and found some decrement in inert gas partial pressure with respect to radial distance. Subsequently, for higher breathing rates, such as $f = 18,20$, we find that the partial pressure of inert gas starts from lower values than the previous rates and remains constant just before reaching the radial boundary of the blood capillary, after which it slightly increases. Simultaneously, we analyzed the radial diffusion of inert gas on the entering position of tissue in Figure 8B. Here for $f = 12$ diffusion of inert gas in tissue decreases, while for $f = 15$ it is constant. But for $f = 18$ and $f = 20$ it increases compared with the partial pressure of inert gas in the blood capillary due to no flux boundary condition. Similarly, at the end of the blood capillary, we calculated the effect of inert gas partial pressure for different values of breathing rates, $f = 12,15,18,20$ per minute, in blood as shown in Figure 8C and in tissue as shown in Figure 8D. Here, we found that the partial pressure of inert gas in both blood and tissue is directly proportional to the breathing rate. This may be due to no flux boundary condition.

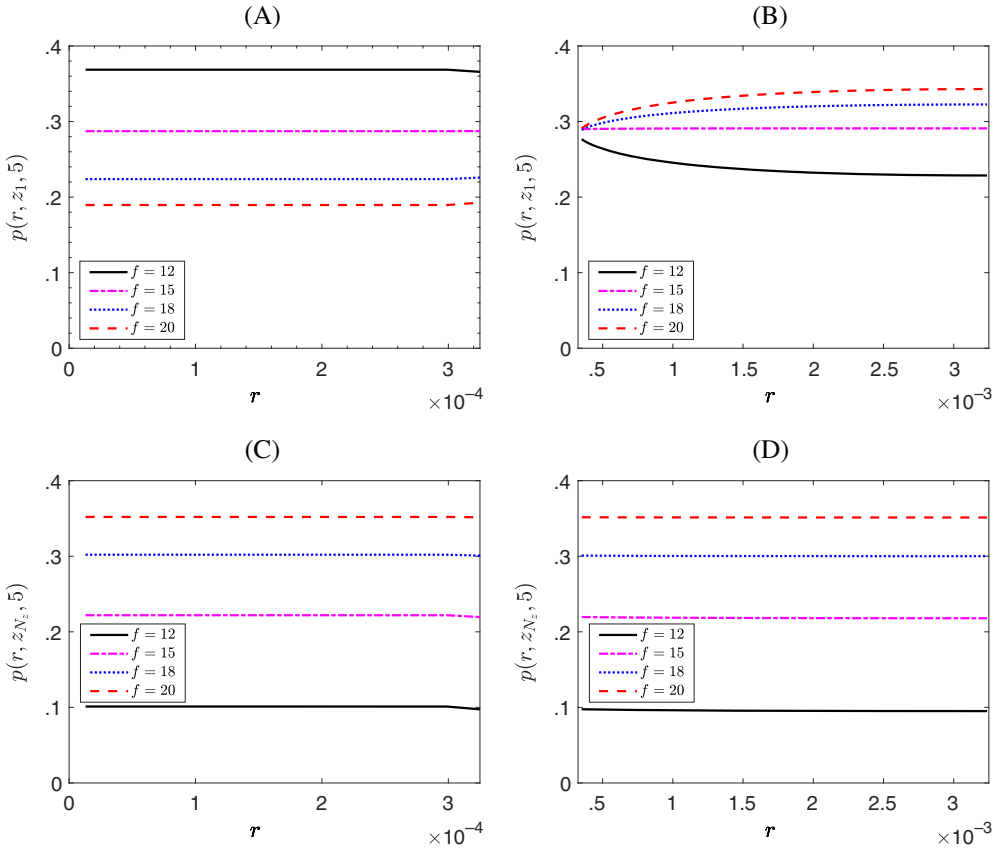

FIGURE 8 Radial effect of breathing frequency $f = 12,15,18,20$ per minute on (A) entering position of blood capillary $p(r_i,z_1,t)$ for $i = 1,2,...,b$ and (B) its surround tissue $p(r_i,z_1,t)$ for $i = b+1,b+2,...,N_r$, also on (C) ending position of blood capillary $p\left(r_i,z_{N_z},t\right)$ for $i = 1,2,...,b$, and (D) its surround tissue $p\left(r_i,z_{N_z},t\right)$ for $i = b+1,b+2,...,N_r$ at $t = 5$.

Under the same conditions, we changed the boundary condition at $r = R_t$ to the homogeneous Dirichlet boundary condition, which was originally a homogeneous Neumann boundary condition. Figure 9 illustrates the radial effects when applying the homogeneous Dirichlet boundary condition. The first noticeable difference is that the partial pressure of inert gas decreased for all frequencies when entering the position of tissue. Such a phenomenon happens at both the entering position of the blood capillary and ending position of blood capillary. Also, lower frequency led to smaller partial pressure at all positions. Lastly, the partial pressure converged to zero at $r = R_t$ as z increased, due to the homogeneous Dirichlet boundary condition.

From the above results, we observed that when inert gas entered the blood capillary, it diffused from blood to tissue, where it became soluble. Due to no flux boundary condition, it accumulated at the tissue boundary, causing a high partial pressure even for the lowest entering arterial pressure difference.

4.5 | Axial effect of initial arterial pressure difference on partial pressure of inert gas

In Figure 10, we observed the effect of initial arterial pressure difference $P_0 = 1,.75,.45,.30,$[29,47] on the center of the blood capillary $p(r_1,z,t)$, axial boundary of the blood $p(r_b,z,t)$ and the tissue $p(r_{N_r},z,t)$ capillaries at $t = 5$ using the numerical values as defined in Table 1.

At the center of the blood capillary $p(r_1,z,t)$ in Figure 10A, we observed that initially, the arterial pressure of inert gas starts from .28 at an initial arterial pressure difference $P_0 = 1$ and tends to decrease with respect to the axial length z. Then we decreased the entering pressure $P_0 = .75$ and observed some decrement of inert gas partial pressure axially. After that, we choose some lower entering pressures, such as $P_0 = .45,.30$ but this time partial pressure of inert gas at the center of the tube however begins from the lower values than previous entering pressures but starts to increase with respect to axial distance.

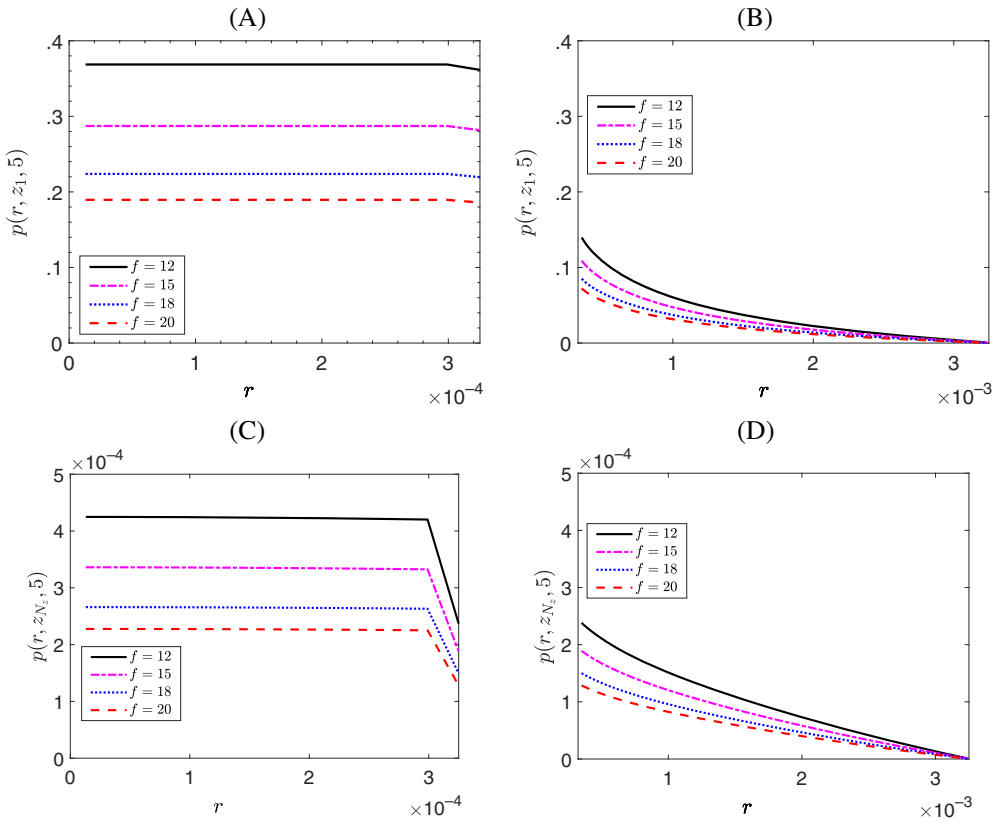

FIGURE 9 Radial effect of breathing frequency $f = 12,15,18,20$ per minute under the homogeneous Dirichlet boundary condition. (A) Entering position of blood capillary $p(r_i,z_1,t)$ for $i = 1,2,...,b$ and (B) its surround tissue $p(r_i,z_1,t)$ for $i = b+1,b+2,...,N_r$, also on (C) ending position of blood capillary $p(r_i,z_{N_z},t)$ for $i = 1,2,...,b$, and (D) its surround tissue $p(r_i,z_{N_z},t)$ for $i = b+1,b+2,...,N_r$ at $t = 5$.

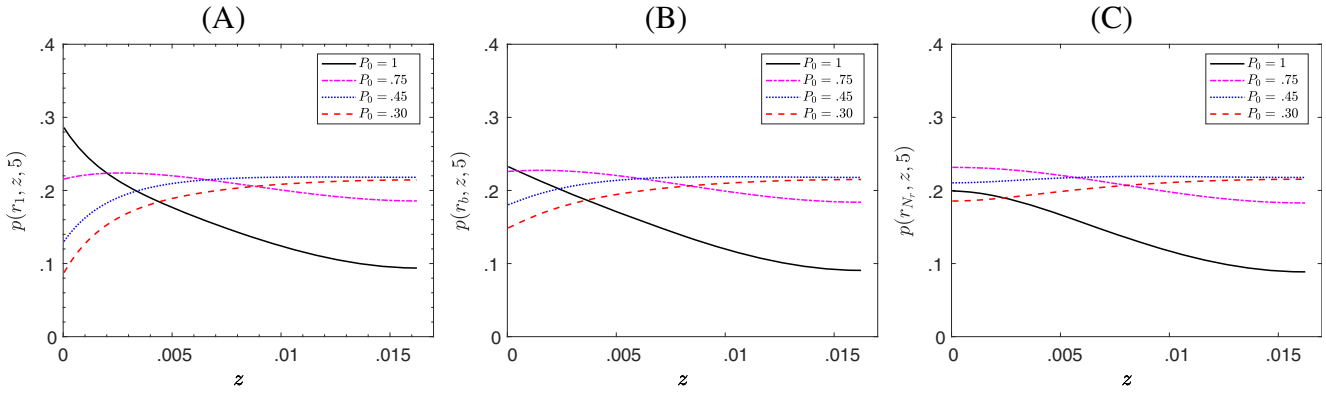

FIGURE 10 Axial effect of initial arterial pressure difference $P_0 = 1,.75,.45,.30$ on (A) the center of blood capillary, $p(r_1,z,t)$, (B) boundary of the blood capillary, $p(r_b,z,t)$, and (C) boundary of the tissue capillary $p(r_{N_r},z,t)$ at $t = 5$.

Then, we analyzed the partial pressure of inert gas at the axial boundary of blood $p(r_b,z,t)$ in Figure 10B and we observed that for the highest entering pressure difference the partial pressure of inert gas has decreasing nature while, as we decrease the pressure difference the partial pressure of inert gas shows increasing nature with respect to axial distance. One more thing is noticeable here the partial pressure of inert gas has lower values than center of tube. In the end, we analyzed the effect of entering pressure difference on the axial boundary of tissue in Figure 10C and found for the highest entering pressure difference the partial pressure of inert gas is lower than the other higher entering pressure difference.

Physiologically, we can conclude that for the lowest entering pressure difference, a lesser amount of inert gas will reach the surrounding tissue of the blood capillary, which will affect less the patient so the appropriate entering pressure to take inert gas should be $P_0 \leq .30$.

4.6 | Radial effect of initial arterial pressure difference on partial pressure of inert gas

In Figure 11, we found effect of initial arterial pressure difference $P_0 = 1,.75,.45,.30$,[29,47] on entering position of blood capillary $p(r_i,z_1,t)$, $i = 1,2,...,b$ and its surround tissue $p(r_i,z_1,t)$, $i = b+1,b+2,...,N_r$ also on ending position of blood capillary $p(r_i,z_{N_z},t)$, $i = 1,2,...,b$ and its surround tissue $p(r_i,z_{N_z},t)$, $i = b+1,b+2,...,N_r$ at $t = 5$. In Figure 11A, we observed that at on the entering point of the blood capillary for an initial arterial pressure difference $P_0 = 1$ the partial pressure of inert gas starts at approximately .3 and then becomes constant just before the radial boundary of the blood capillary. After that, it slightly leans down. Then we decreased the entering pressure $P_0 = .75$ and found some decrement in inert gas partial pressure with respect to radial distance. After that, we chose some lower entering pressures such that $P_0 = .45,.30$ and found partial pressure of inert gas starts from a lower value than the previous one and remains constant just before the radial boundary of the blood capillary after that it slightly gets up.

Simultaneously, we analyzed the radial diffusion of inert gas at the entering position of tissue in Figure 11B, here for $P_0 = 1$ the diffusion of inert gas in tissue decreases while for $P_0 = .75$ it is constant. However, for $P_0 = .45$ and $P_0 = .30$ it increases compared with the partial pressure of inert gas in the blood capillary possibly due to no flux boundary condition. Similarly, at the end of the blood capillary, we calculated the effect of inert gas partial pressure for different values of $P_0 = 1,.75,.45,.30$ in blood, as shown in Figure 11C and in tissue as in Figure 11D. Here, we found that the partial pressure of inert gas in both blood and tissue is inversely proportional to the arterial pressure difference due to the no flux boundary condition.

From the above results, we observed that when inert gas enters the blood capillary it diffuses from blood to tissue where it gets soluble and due to no flux boundary condition, it accumulates at the tissue boundary and causes high partial pressure even for the lowest entering arterial pressure difference.

4.7 | Effect of initial velocity of blood on arterial/venous blood partial pressure

In Figure 12, we investigated the impact of the initial velocity of blood on arterial (P_a) and venous (P_v) blood partial pressure. We examined this effect for four different values of $w = .01,.03,.05$ (velocity varies from $.01 - .2$ mm/s[48]), and

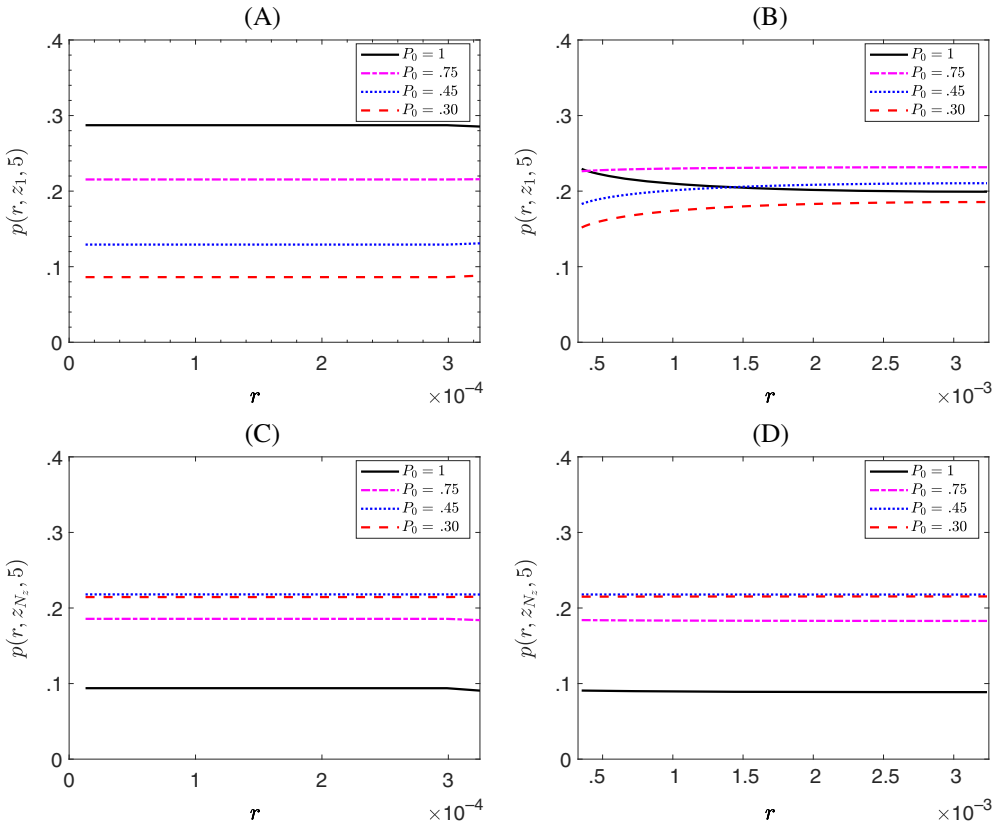

FIGURE 11 Radial effect of initial arterial pressure difference $P_0 = 1,.75,.45,.30$ on (A) entering position of blood capillary $p(r_i, z_1, t)$ for $i = 1, 2, ..., b$ and (B) its surround tissue $p(r_i, z_1, t)$ for $i = b+1, b+2, ..., N_r$, also on (C) ending position of blood capillary $p(r_i, z_{N_z}, t)$ for $i = 1, 2, ..., b$, and (D) its surround tissue $p(r_i, z_{N_z}, t)$ for $i = b+1, b+2, ..., N_r$ at $t = 5$.

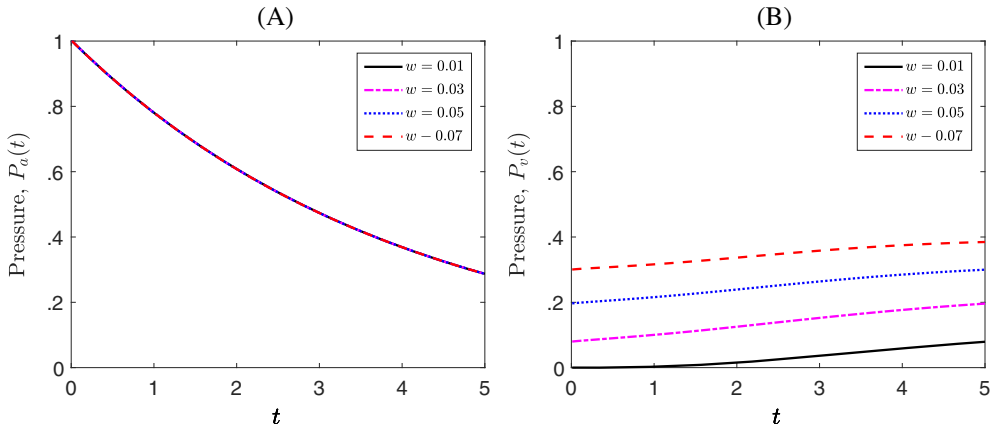

FIGURE 12 Effect of velocity on (A) arterial and (B) venous blood partial pressure P_a and P_v for velocity $w = .01,.03,.05$ at time $t = 5$.

.07. Our findings revealed that due to the exponential decay nature of arterial pressure, it exponentially decreases over time as shown in Figure 12A. However, we observed no significant effect of changes in velocity on arterial blood partial pressure (P_a). On the other hand, in Figure 12B, when we increased the velocity of blood flow, the value of venous blood partial pressure (P_v) increased proportionally. This indicates that arterial pressure is primarily governed by factors other than blood velocity. While venous blood partial pressure has a direct relationship with blood velocity. Higher blood flow velocity contributes to an elevation in venous blood pressure, suggesting that velocity plays a more significant role in the venous system compared with the arterial system.

The pressure profile in both arterial and venous blood at $T = 1, 3$, and 5 is illustrated in Figure 13. We can see that the results agree with the ones in Figure 12.

4.8 | Analysis of the effect of nitrous oxide (N_2O) and oxygen (O_2) on venous partial pressure

In Figure 14, we investigated the impact of nitrous oxide (N_2O) and oxygen (O_2) on venous (P_v) blood partial pressure at $t = 5$ by taking the solubility and diffusivity of N_2O and O_2 as defined in Table 1. We found that due to the inhalation of the anesthetic gas N_2O, the partial pressure of venous (P_v) blood had lower values compared with the inhalation of oxygen O_2. This is due to the higher solubility and diffusivity of N_2O in blood and tissue as compared with O_2, which shows that N_2O stays inside blood and tissue for a longer time and affects the venous pressure of blood to a greater extent than O_2. In the future, we will apply a least-squares method to find optimal parameter values.[49]

Also, to visualize the effect of N_2O and O_2 on the pressure profiles inside the blood capillary, we illustrate the profiles in Figure 15 at $T = 1, 3$, and 5. We can see that pressure profiles align with the results presented in Figure 14.

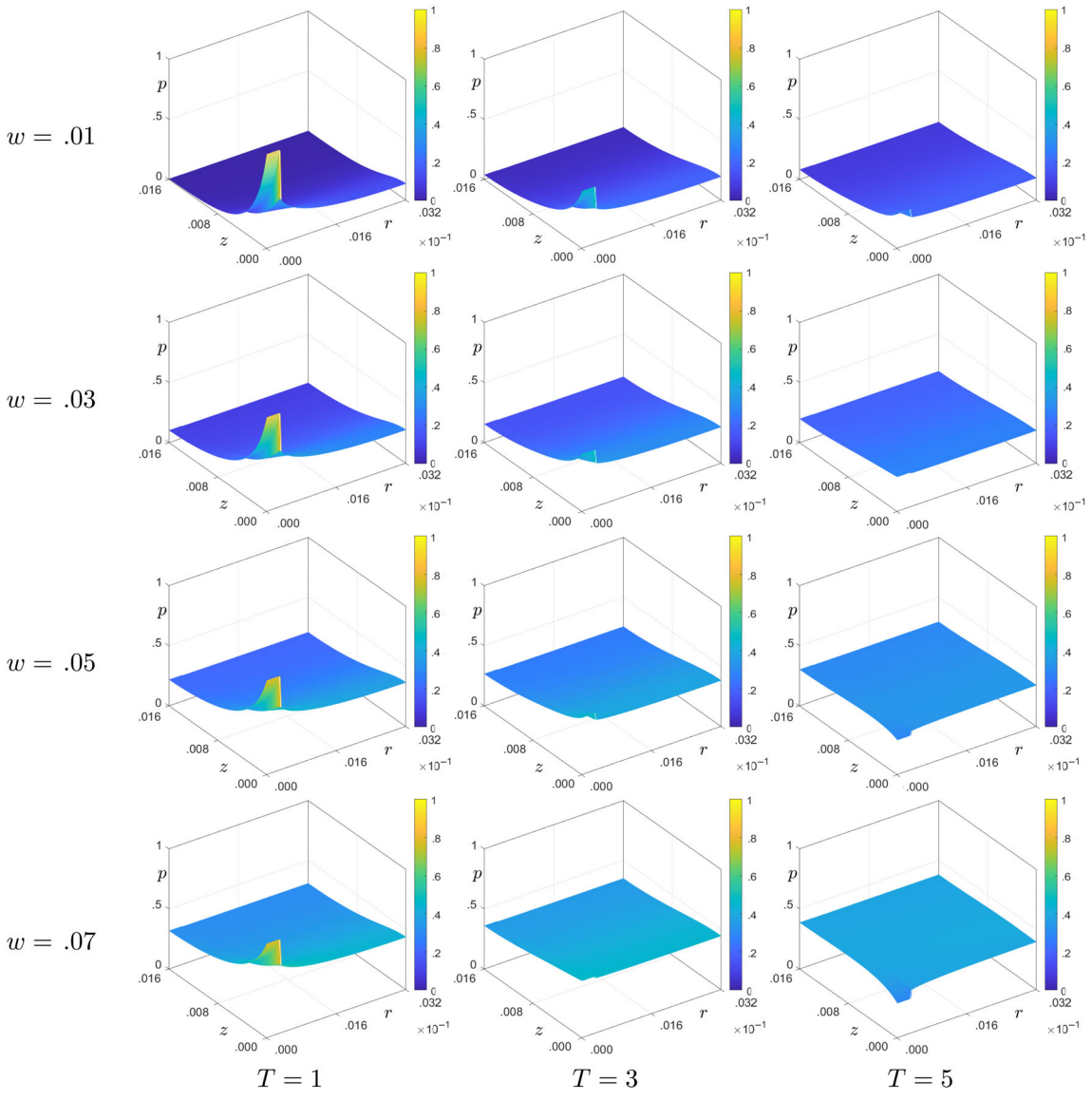

FIGURE 13 Pressure profile at $T = 1, 3$, and 5 with different values of w.

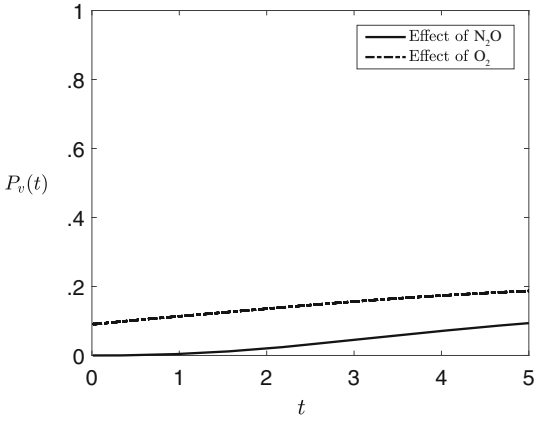

FIGURE 14 Nitrous oxide (N_2O) and oxygen (O_2) on venous (P_v) blood partial pressure at $t = 5$.

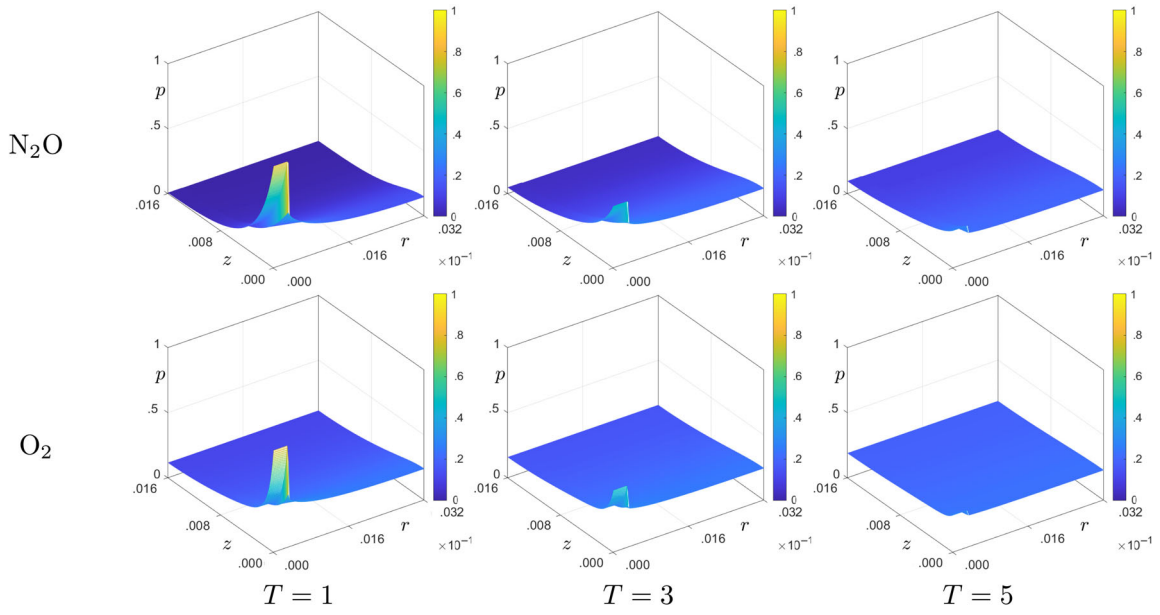

FIGURE 15 Pressure profiles of N_2O and O_2 at $T = 1, 3$, and 5.

5 | CONCLUSION

This study utilized a fast and accurate OSM to examine how inert gas affects the partial pressure of alveolar and venous blood. The OSM allowed for the separation of governing equations into smaller sub-problems, providing insights into inert gas transport between blood capillaries and tissue. The governing equations underwent discretization using a fully implicit finite difference approach, thereby improving computational efficiency. Validation of the scheme is done by performing some tests, which was also done by previous study,[17] and found very much similarity in the results computational. The model considered convection-diffusion in blood and diffusion in tissue through PDEs. Various parameters such as initial arterial pressure, breathing frequency, blood flow velocity, solubility, and diffusivity were explored to understand their impact on the partial pressure of inert gas in blood and tissue.

In conclusion, the physiological findings of this study provide valuable insights into the impact of frequency rate and entering pressure difference on the distribution of inert gas to the surrounding tissue of blood capillaries. It is evident that a lower frequency rate ($f \leq 12/60$) results in a reduced amount of inert gas reaching the tissue, minimizing its effects on patients. Similarly, an appropriate entering pressure ($P_0 \leq .30$) ensures a controlled distribution of inert gas to the surrounding tissue, further reducing potential adverse effects. The study also elucidates the role of blood velocity, which shows venous blood pressure exhibits a direct relationship with blood velocity. Moreover, simulation results

demonstrated that the high solubility and diffusivity of anesthetic inert gas contributed to its prolonged presence in both blood and tissue, resulting in lower partial pressure in venous blood.

Overall, this study contributes valuable physiological insights with potential implications for medical diagnostics and therapies related to the gas exchange process. However, this study has certain constraints. Subsequent research should focus on examining more complex geometries, and additional investigation is necessary to comprehend the impacts of anesthesia or inert gas on individuals across different age groups, as well as gas exchange in patients with cardiovascular or pulmonary conditions.

ACKNOWLEDGMENTS

The first author (Jyoti) was supported by Brain Pool program funded by the National Research Foundation of Korea (NRF) funded by the Ministry of Science and ICT (2022H1D3A2A02081237). The corresponding author (J.S. Kim) was supported by the National Research Foundation (NRF), Korea, under project BK21 FOUR. The authors express their gratitude to the reviewers for providing valuable feedback during the revision process of this article.

CONFLICT OF INTEREST STATEMENT

The authors declare no conflict of interest.

DATA AVAILABILITY STATEMENT

Data sharing is not applicable to this article as no new data were created or analyzed in this study.

ORCID

Junseok Kim https://orcid.org/0000-0002-0484-9189

REFERENCES

1. Hedenstierna G, Rothen HU. Respiratory function during anesthesia: effects on gas exchange. *Compr Physiol*. 2011;2(1):69-96.
2. Kumar R, Tokas S, Hadda V, Rakshit D, Sarkar J. Numerical modeling and development of a dual lung simulator using partitioned fluid–structure interaction approach for ventilator testing. *Int J Numer Methods Biomed Eng*. 2022;38(7):e3607.
3. Strandberg Å, Tokics L, Brismar B, Lundquist H, Hedenstierna G. Atelectasis during anaesthesia and in the postoperative period. *Acta Anaesthesiol Scand*. 1986;30(2):154-158.
4. Faro AFL, Battistini A, Pirani F, et al. Fatal inhalation of nitrogen inside a closed environment: toxicological issues about the cause of death. *Forensic Sci Int*. 2019;302:109871.
5. Harding BE, Wolf BC. Case report of suicide by inhalation of nitrogen gas. *Am J Forensic Med Pathol*. 2008;29(3):235-237.
6. Kim YE, Lee D, Kim M, Hwang H. Brain MRI findings of nitrogen gas inhalation for suicide attempt: a case report. *Investig Magn Reson Imaging*. 2017;21(4):264-268.
7. Pozin N, Montesantos S, Katz I, Pichelin M, Vignon-Clementel I, Grandmont C. A tree-parenchyma coupled model for lung ventilation simulation. *Int J Numer Methods Biomed Eng*. 2017;33(11):e2873.
8. Carfora A, Petrella R, Ambrosio G, et al. Helium suicide, a rapid and painless asphyxia: toxicological findings. *Toxics*. 2022;10(8):424.
9. Cuypers E, Rosier E, Loix S, et al. Medical findings and toxicological analysis in infant death by balloon gas asphyxia: a case report. *J Anal Toxicol*. 2017;41(4):347-349.
10. Nithiarasu P, Sazonov I. A novel modelling approach to energy transport in a respiratory system. *Int J Numer Methods Biomed Eng*. 2017;33(10):e2854.
11. Brouqui P, Amrane S, Million M, et al. Asymptomatic hypoxia in COVID-19 is associated with poor outcome. *Int J Infect Dis*. 2021;102:233-238.
12. Kannan R, Chen ZJ, Singh N, et al. A quasi-3D wire approach to model pulmonary airflow in human airways. *Int J Numer Methods Biomed Eng*. 2017;33(7):e2838.
13. Sirohiya P, Elavarasi A, Sagiraju HKR, et al. Silent hypoxia in coronavirus disease-2019: is it more dangerous?—a retrospective cohort study. *Lung India*. 2022;39(3):247-253.
14. Wu W, Ueng J, Chai C. Effects of asphyxia on arterial blood pressure, formation of nitric oxide in medulla and blood parameters in the cat. *Chin J Physiol*. 2005;48(1):51-56.
15. Sugiharto AF, Firdausi RA, Safitry O. The effects of declined oxygen levels on hypoxia symptoms and blood gases: an experimental study. *J Phys Conf Ser*. 2018;1073(4):042023.
16. Kori J, Pratibha Effect of first order chemical reactions through tissue-blood interface on the partial pressure distribution of inhaled gas. *Comput Methods Biomech Biomed Engin*. 2022;25(1):84-96.
17. Whiteley JP, Gavaghan DJ, Hahn CEW. Modelling inert gas exchange in tissue and mixed-venous blood return to the lungs. *J Theor Biol*. 2001;209(4):431-443.
18. Rhoades R, Bell DR. *Medical Physiology: Principles for Clinical Medicine*. 4th ed. Lippincott Williams & Wilkins; 2013.

19. Chalkias A, Laou E, Papagiannakis N, et al. Determinants of venous return in steady-state physiology and asphyxia-induced circulatory shock and arrest: an experimental study. *Intensive Care Med Exp*. 2022;10(1):13.
20. Hedenstierna G, Tokics L, Scaramuzzo G, Rothen HU, Edmark L, Öhrvik J. Oxygenation impairment during anesthesia: influence of age and body weight. *Anesthesiology*. 2019;131(1):46-57.
21. Nassar B, Mallat J. Usefulness of venous-to-arterial partial pressure of CO2 difference to assess oxygen supply to demand adequacy: effects of dobutamine. *J Thorac Dis*. 2019;11(11):S1574-S1578.
22. Polak AG. Algebraic approximation of the distributed model for the pressure drop in the respiratory airways. *Int J Numer Methods Biomed Eng*. 2022;38(9):e3632.
23. Victor MH Jr, Maximo MR, Matsumoto MM, Pereira SM, Tucci MR. Mixed-integer quadratic programming approach for noninvasive estimation of respiratory effort profile during pressure support ventilation. *Int J Numer Methods Biomed Eng*. 2023;39(1):e3668.
24. Oakes JM, Shadden SC, Grandmont C, Vignon-Clementel IE. Aerosol transport throughout inspiration and expiration in the pulmonary airways. *Int J Numer Methods Biomed Eng*. 2017;33(9):e2847.
25. Ren S, Cai M, Shi Y, Xu W, Zhang XD. Influence of bronchial diameter change on the airflow dynamics based on a pressure-controlled ventilation system. *Int J Numer Methods Biomed Eng*. 2018;34(3):e2929.
26. Hedenstierna G, Rothen HU. Atelectasis formation during anesthesia: causes and measures to prevent it. *J Clin Monit Comput*. 2000;16:329-335.
27. Singh MP, Sharan M, Sud I. The process of gas exchange in systemic circulation in a hyperbaric environment: an analytical approach. *Math Med Biol A J IMA*. 1988;5(4):281-301.
28. Sharan M, Selvakumar S, Singh MP. Mathematical model for the computation of alveolar partial pressure of carbon monoxide. *Int J Biomed Comput*. 1990;26(3):135-147.
29. Sharan M, Singh B, Singh MP, Kumar P. Finite-element analysis of oxygen transport in the systemic capillaries. *Math Med Biol A J IMA*. 1991;8(2):107-123.
30. Melo MV, Loeppky JA, Caprihan A, Luft UC. Alveolar ventilation to perfusion heterogeneity and diffusion impairment in a mathematical model of gas exchange. *Comput Biomed Res*. 1993;26(2):103-120.
31. Baker AB, Farmery AD. Inert gas transport in blood and tissues. *Compr Physiol*. 2011;1(2):569-592.
32. Ravshanov N, Muradov F, Akhmedov D. Operator splitting method for numerical solving the atmospheric pollutant dispersion problem. *J Phys Conf Ser*. 2020;1441(1):012164.
33. Valocchi AJ, Malmstead M. Accuracy of operator splitting for advection-dispersion-reaction problems. *Water Resour Res*. 1992;28(5):1471-1476.
34. Liu C, Wang C, Wang Y, Wise SM. Convergence analysis of the variational operator splitting scheme for a reaction-diffusion system with detailed balance. *SIAM J Numer Anal*. 2022;60(2):781-803.
35. Gavaghan DJ, Hahn CEW. A mathematical evaluation of the alveolar amplitude response technique. *Respir Physiol*. 1995;102(1):105-120.
36. Zwart A, Seagrave RC, Van Dieren A. Ventilation-perfusion ratio obtained by a noninvasive frequency response technique. *J Appl Physiol*. 1976;41(3):419-424.
37. Chen M, Ham S, Choi Y, Kim H, Kim J. Pattern dynamics of a harvested predator-prey model. *Chaos Solitons Fractals*. 2023;176:114153.
38. Nunn JF. Pulmonary ventilation: mechanisms and the work of breathing. *Nunn's Applied Respiratory Physiology*. 4th ed. Butterworth-Heinemann; 1993:117-134.
39. Kawashiro T, Carles AC, Perry SF, Piiper J. Diffusivity of various inert gases in rat skeletal muscle. *Pflugers Arch*. 1975;359:219-230.
40. McCarthy M, Shelledy DC. Physical assessment. In: Shelledy DC, Peters JL, eds. *Respiratory Care: Patient Assessment and Care Plan Development*. Jones and Bartlett Learning; 2016:137-186.
41. Scott JB, Kaur R. Monitoring breathing frequency, pattern, and effort. *Respir Care*. 2020;65(6):793-806.
42. Cavalcante AN, Martin YN, Sprung J, Imsirovic J, Weingarten TN. Low minute ventilation episodes during anesthesia recovery following intraperitoneal surgery as detected by a non-invasive respiratory volume monitor. *J Clin Monit Comput*. 2018;32:929-935.
43. Pleil JD, Wallace MAG, Davis MD, Matty CM. The physics of human breathing: flow, timing, volume, and pressure parameters for normal, on-demand, and ventilator respiration. *J Breath Res*. 2021;15(4):042002.
44. Ball L, Costantino F, Fiorito M, Amodio S, Pelosi P. Respiratory mechanics during general anaesthesia. *Ann Transl Med*. 2018;6(19):379.
45. Izumi Y, Kochi T, Isono S, Ide T, Mizuguchi T. Breathing pattern and respiratory mechanics in sevoflurane-anesthetized humans. *J Anesth*. 1990;4:343-349.
46. Rocco PRM, Zin WA. Respiratory effects of anesthesia. In: Gullo A, ed. *Anaesthesia, Pain, Intensive Care and Emergency Medicine*. Springer; 2002.
47. Whiteley JP, Gavaghan DJ, Hahn CE. Mathematical modelling of oxygen transport to tissue. *J Math Biol*. 2002;44:503-522.
48. Lu Y, Michel CC, Wang W. Inert gas clearance from tissue by co-currently and counter-currently arranged microvessels. *J Appl Physiol*. 2012;113(3):487-497.
49. Ham S, Kwak S, Lee C, Lee G, Kim J. A second-order time-accurate unconditionally stable method for a gradient flow for the Modica–Mortola functional. *J Sci Comput*. 2023;95(2):63.
50. Kwak S, Kang S, Ham S, Hwang Y, Lee G, Kim J. An unconditionally stable difference scheme for the two-dimensional modified Fisher–Kolmogorov–Petrovsky–Piscounov equation. *J Math*. 2023;2023:1-14.

How to cite this article: Jyoti, Kwak S, Ham S, Hwang Y, Kang S, Kim J. Analysis of the effect of inert gas on alveolar/venous blood partial pressure by using the operator splitting method. *Int J Numer Meth Biomed Engng*. 2024;40(8):e3839. doi:10.1002/cnm.3839

APPENDIX A: Solution process by using operator splitting method

We describe the proposed solution algorithm by using the operator splitting method.[49,50]

- Step 1: Discretization in r-direction,

First we consider the r-direction equation for $k=1$ and $i=1,...,N_r$. Since $P_{i1}^{n+\frac{1}{2}}$ are given in Equation (4) for $i=1,...,b-1$, we calculate $P_{b1}^{n+\frac{1}{2}}, P_{b+1,1}^{n+\frac{1}{2}},...,P_{N_r1}^{n+\frac{1}{2}}$, where $P_{b1}^{n+\frac{1}{2}}$ is the pressure on the interface at point r_b.

Let us consider the continuous flux condition defined in Equation (13):

$$\alpha_b D_b\left(\frac{P_{b1}^{n+\frac{1}{2}}-P_{b-1,1}^{n}}{\Delta r}\right)=\alpha_t D_t\left(\frac{P_{b+1,1}^{n+\frac{1}{2}}-P_{b1}^{n+\frac{1}{2}}}{\Delta r}\right). \tag{A1}$$

We can rewrite the above equation as,

$$(\alpha_b D_b+\alpha_t D_t)P_{b1}^{n+\frac{1}{2}}-\alpha_t D_t P_{b+1,1}^{n+\frac{1}{2}}=\alpha_b D_b P_{b-1,1}^{n}. \tag{A2}$$

Now, for $i=b+1,...,N_r-1$ where $P_{i1}^{n+\frac{1}{2}}$ is in the tissue, the discretized Equation (11) for $R_b<r<R_t$ can be written as,

$$\frac{P_{i1}^{n+\frac{1}{2}}-P_{i1}^{n}}{\Delta t}=\frac{D_t}{r_i}\left[\left(r_i+\frac{\Delta r}{2}\right)\left(\frac{P_{i+1,1}^{n+\frac{1}{2}}-P_{i1}^{n+\frac{1}{2}}}{\Delta r^2}\right)-\left(r_i-\frac{\Delta r}{2}\right)\left(\frac{P_{i1}^{n+\frac{1}{2}}-P_{i-1,1}^{n+\frac{1}{2}}}{\Delta r^2}\right)\right], \tag{A3}$$

which can be written in an implicit form with $\alpha_1=\frac{D_t\Delta t}{\Delta r^2}$ as,

$$-\alpha_1\left(1-\frac{\Delta r}{2r_i}\right)P_{i-1,1}^{n+\frac{1}{2}}+(1+2\alpha_1)P_{i1}^{n+\frac{1}{2}}-\alpha_1\left(1+\frac{\Delta r}{2r_i}\right)P_{i+1,1}^{n+\frac{1}{2}}=P_{i1}^{n}. \tag{A4}$$

For $i=N_r$, we apply the homogeneous Neumann boundary condition $P_{N_r+1,1}=P_{N_r1}$ on Equation (A4). Then,

$$-\alpha_1\left(1-\frac{\Delta r}{2r_{N_r}}\right)P_{N_r-1,1}^{n+\frac{1}{2}}+\left[1+\alpha_1\left(1-\frac{\Delta r}{2r_{N_r}}\right)\right]P_{N_r1}^{n+\frac{1}{2}}=P_{N_r1}^{n}. \tag{A5}$$

From Equations (A2), (A4), and (A5), we can derive the following matrix form,

$$A_1\mathbf{P}_1^{n+\frac{1}{2}}=\mathbf{P}_1^{n},$$

where A_1 is an $(N_r-b+1)\times(N_r-b+1)$ matrix,

$$A_1 = \begin{pmatrix} 1+\frac{\alpha_t D_t}{\alpha_b D_b} & -\alpha_t D_t & 0 & \cdots & 0 & 0 & 0 \\ -\alpha_1\left(1-\frac{\Delta r}{2r_{b+1}}\right) & (1+2\alpha_1) & -\alpha_1\left(1+\frac{\Delta r}{2r_{b+1}}\right) & 0 & \cdots & 0 & 0 \\ 0 & -\alpha_1\left(1-\frac{\Delta r}{2r_{b+2}}\right) & (1+2\alpha_1) & -\alpha_1\left(1+\frac{\Delta r}{2r_{b+2}}\right) & 0 & \cdots & 0 \\ \vdots & \vdots & \ddots & \ddots & \ddots & \vdots & \vdots \\ 0 & \cdots & 0 & -\alpha_1\left(1-\frac{\Delta r}{2r_{N_r-2}}\right) & (1+2\alpha_1) & -\alpha_1\left(1+\frac{\Delta r}{2r_{N_r-2}}\right) & 0 \\ 0 & 0 & \cdots & 0 & -\alpha_1\left(1-\frac{\Delta r}{2r_{N_r-1}}\right) & (1+2\alpha_1) & -\alpha_1\left(1+\frac{\Delta r}{2r_{N_r-1}}\right) \\ 0 & 0 & 0 & \cdots & 0 & -\alpha_1\left(1-\frac{\Delta r}{2r_i}\right) & 1+\alpha_1\left(1-\frac{\Delta r}{2r_{N_r}}\right) \end{pmatrix},$$

$$\mathbf{P}_1^{n+\frac{1}{2}} = \left(P_{b1}^{n+\frac{1}{2}}, \cdots, P_{N_r 1}^{n+\frac{1}{2}}\right)^T \text{ and } \mathbf{P}_1^n = \left(P_{b1}^n, \cdots, P_{N_r 1}^n\right)^T. \tag{A6}$$

For $k = 2, 3, ..., N_z$, we will find $P_{ik}^{n+\frac{1}{2}}$ for $i = 1, ..., b-1$ as,

$$\frac{P_{ik}^{n+\frac{1}{2}} - P_{ik}^n}{\Delta t} = \frac{D_b}{r_i}\left[\left(r_i + \frac{\Delta r}{2}\right)\left(\frac{P_{i+1,k}^{n+\frac{1}{2}} - P_{ik}^{n+\frac{1}{2}}}{\Delta r^2}\right) - \left(r_i - \frac{\Delta r}{2}\right)\left(\frac{P_{ik}^{n+\frac{1}{2}} - P_{i-1,k}^{n+\frac{1}{2}}}{\Delta r^2}\right)\right], \tag{A7}$$

which can be rewritten in an implicit form with $\alpha_2 = \frac{D_b \Delta t}{\Delta r^2}$ as,

$$-\alpha_2\left(1-\frac{\Delta r}{2r_i}\right)P_{i-1,k}^{n+\frac{1}{2}} + (1+2\alpha_2)P_{ik}^{n+\frac{1}{2}} - \alpha_2\left(1+\frac{\Delta r}{2r_i}\right)P_{i+1,k}^{n+\frac{1}{2}} = P_{ik}^n, \text{ for } i = 2, 3, ..., b-1. \tag{A8}$$

Equation (A8) works as usual except at $i = 1$ due to symmetric boundary condition. Equation (A8) converts for $i = 1$ as,

$$\left[1+\alpha_2\left(\frac{1+\Delta r}{2r_i}\right)\right]P_{ik}^{n+\frac{1}{2}} - \alpha_2\left(\frac{1+\Delta r}{2r_i}\right)P_{i+1,k}^{n+\frac{1}{2}} = P_{ik}^n. \tag{A9}$$

We discretize continuous flux condition at $i = b$, which is defined in Equation (13) as,

$$\alpha_b D_b\left(\frac{P_{bk}^{n+\frac{1}{2}} - P_{b-1,k}^{n+\frac{1}{2}}}{\Delta r}\right) = \alpha_t D_t\left(\frac{P_{b+1,k}^{n+\frac{1}{2}} - P_{bk}^{n+\frac{1}{2}}}{\Delta r}\right). \tag{A10}$$

Then we rewrite as,

$$\alpha_b D_b P_{b-1,k}^{n+\frac{1}{2}} + (\alpha_b D_b + \alpha_t D_t)P_{bk}^{n+\frac{1}{2}} - \alpha_t D_t P_{b+1,k}^{n+\frac{1}{2}} = 0, \tag{A11}$$

After that we can get value of $P_{ik}^{n+\frac{1}{2}}$ in tissue phase from $i = b+1, b+2, ..., N_r-1, N_r$ as defined in Equations (A3)–(A5). By Equations (A4), (A5), and (A8)–(A11), we can derive the following matrix form,

$$A_2 \mathbf{P}_k^{n+\frac{1}{2}} = \mathbf{P}_k^n,$$

$$A_2 = \begin{pmatrix} 1+\alpha_2\left(1+\frac{\Delta r}{2r_i}\right) & -\alpha_2\left(1+\frac{\Delta r}{2r_i}\right) & 0 & \cdots & 0 & 0 & 0 \\ -\alpha_2\left(1-\frac{\Delta r}{2r_i}\right) & 1+2\alpha_2 & -\alpha_2\left(1+\frac{\Delta r}{2r_i}\right) & 0 & \cdots & 0 & 0 \\ \vdots & \vdots & \ddots & \ddots & \ddots & \vdots & \vdots \\ 0 & -\alpha_b D_b & \alpha_b D_b+\alpha_t D_t & -\alpha_t D_t & \cdots & 0 & 0 \\ 0 & 0 & -\alpha_1\left(1-\frac{\Delta r}{2r_{b+1}}\right) & (1+2\alpha_1) & -\alpha_1\left(1+\frac{\Delta r}{2r_{b+1}}\right) & 0 & 0 \\ \vdots & \vdots & \ddots & \ddots & \ddots & \vdots & \vdots \\ 0 & \cdots & 0 & -\alpha_1\left(1-\frac{\Delta r}{2r_{N_r-2}}\right) & (1+2\alpha_1) & -\alpha_1\left(1+\frac{\Delta r}{2r_{N_r-2}}\right) & 0 \\ 0 & 0 & \cdots & 0 & -\alpha_1\left(1-\frac{\Delta r}{2r_{N_r-1}}\right) & (1+2\alpha_1) & -\alpha_1\left(1+\frac{\Delta r}{2r_{N_r-1}}\right) \\ 0 & 0 & 0 & \cdots & 0 & -\alpha_1\left(1-\frac{\Delta r}{2r_i}\right) & 1+\alpha_1\left(1-\frac{\Delta r}{2r_{N_r}}\right) \end{pmatrix},$$

where A_2 is an $N_r \times N_r$ matrix, and,

$$\mathbf{P}_k^{n+\frac{1}{2}} = \left(P_{1k}^{n+\frac{1}{2}}, \cdots, P_{N_r k}^{n+\frac{1}{2}}\right)^T \text{ and } \mathbf{P}_k^n = \left(P_{1k}^n, \cdots, P_{N_r k}^n\right)^T, \text{for } k = 2, ..., N_z. \tag{A12}$$

- Step 2: Discretization in z-direction for $i = 1, ..., N_r$.

We discretize Equation (14) as follows:

$$\frac{P_{ik}^{n+1} - P_{ik}^{n+\frac{1}{2}}}{\Delta t} = \begin{cases} D_b \dfrac{P_{i,k-1}^{n+1} - 2P_{ik}^{n+1} + P_{i,k+1}^{n+1}}{\Delta z^2} - w\dfrac{P_{ik}^{n+1} - P_{i,k-1}^{n+1}}{\Delta z}, & \text{for } i = 1, ..., b-1 \\ D_t \dfrac{P_{i,k-1}^{n+1} - 2P_{ik}^{n+1} + P_{i,k+1}^{n+1}}{\Delta z^2}, & \text{for } i = b+1, ..., N_r. \end{cases} \tag{A13}$$

First, we consider the case where $i = 1, ..., b-1$ and write Equation (A13) as follows,

$$\alpha_3 P_{i,k-1}^{n+1} + \beta_3 P_{ik}^{n+1} + \gamma_3 P_{i,k+1}^{n+1} = P_{ik}^{n+\frac{1}{2}}, \tag{A14}$$

where,

$$\alpha_3 = -\frac{D_b}{\Delta z^2} - \frac{w}{\Delta z},\ \beta_3 = \frac{1}{\Delta t} + \frac{2D_b}{\Delta z^2} + \frac{w}{\Delta z},\ \gamma_3 = -\frac{D_b}{\Delta z^2}. \tag{A15}$$

Then, we can obtain the following relational expressions at $n+1$ and $n+\frac{1}{2}$ for $k = 1, ..., N_z$.

$$P_{ik}^{n+1} = P_{i0}^{n+\frac{1}{2}}, \text{for } k = 1, \tag{A16}$$

$$\beta_3 P_{ik}^{n+1} + \gamma_3 P_{i,k+1}^{n+1} = \frac{1}{\Delta t} P_{ik}^{n+\frac{1}{2}} - \alpha_3 P_{i0}^{n+\frac{1}{2}}, \text{for } k = 2, \tag{A17}$$

$$\alpha_3 P_{i,k-1}^{n+1} + \beta_3 P_{ik}^{n+1} + \gamma_3 P_{i,k+1}^{n+1} = \frac{1}{\Delta t} P_{ik}^{n+\frac{1}{2}}, \text{ for } k = 3, ..., N_z - 1, \tag{A18}$$

$$\alpha_3 P_{i,k-1}^{n+1} + (\beta_3 + \gamma_3) P_{ik}^{n+1} = \frac{1}{\Delta t} P_{ik}^{n+\frac{1}{2}} \text{ for } k = N_z. \tag{A19}$$

here, $P_{ik}^{n+\frac{1}{2}}$ are given as the Dirichlet boundary condition for blood Equation (4) at $k=1$ and the homogeneous Neumann boundary condition is applied at $k=N_z$. By using Equations (A14)–(A19), we can derive the following matrix form,

$$B_1 \mathbf{P}_i^{n+1} = \mathbf{P}_i^{n+\frac{1}{2}},$$

where B_1 is an $N_z \times N_z$ matrix,

$$B_1 = \begin{pmatrix} 1 & 0 & 0 & \cdots & 0 & 0 & 0 \\ 0 & \beta_3 & \gamma_3 & 0 & \cdots & 0 & 0 \\ 0 & \alpha_3 & \beta_3 & \gamma_3 & \cdots & 0 & 0 \\ 0 & 0 & \alpha_3 & \beta_3 & \gamma_3 & \cdots & 0 \\ \vdots & \vdots & \ddots & \ddots & \ddots & \vdots & \vdots \\ 0 & 0 & \cdots & 0 & \alpha_3 & \beta_3 & \gamma_3 \\ 0 & 0 & 0 & \cdots & 0 & \alpha_3 & \beta_3 + \gamma_3 \end{pmatrix},$$

and

$$\mathbf{P}_i^{n+1} = \left(P_{i1}^{n+1}, \cdots, P_{iN_z}^{n+1}\right)^T, \text{for } i = 1, 2, ..., b-1 \text{ and } \mathbf{P}_i^{n+\frac{1}{2}} = \left(P_{i1}^{n+\frac{1}{2}}, \cdots, P_{iN_z}^{n+\frac{1}{2}}\right)^T.$$

For $i = b+1, ..., N_r$, Equation (A13) written as follows,

$$\alpha_4 P_{i,k-1}^{n+1} + \beta_4 P_{ik}^{n+1} + \gamma_4 P_{i,k+1}^{n+1} = P_{ik}^{n+\frac{1}{2}}, \tag{A20}$$

where

$$\alpha_4 = -\frac{D_t}{\Delta z^2},\ \beta_4 = \frac{1}{\Delta t} + \frac{2D_t}{\Delta z^2},\ \gamma_4 = -\frac{D_t}{\Delta z^2}. \tag{A21}$$

Then, we can obtain the following relational expressions at $n+1$ and $n+\frac{1}{2}$ for $k = 1, ..., N_z$,

$$(\alpha_4 + \beta_4) P_{ik}^{n+1} + \gamma_4 P_{i,k+1}^{n+1} = \frac{1}{\Delta t} P_{ik}^{n+\frac{1}{2}}, \text{for } k = 1, \tag{A22}$$

$$\alpha_4 P_{i,k-1}^{n+1} + \beta_4 P_{ik}^{n+1} + \gamma_4 P_{i,k+1}^{n+1} = \frac{1}{\Delta t} P_{ik}^{n+\frac{1}{2}}, \text{for } i = 1, ..., b-1, \tag{A23}$$

$$\alpha_4 P_{i,k-1}^{n+1} + (\beta_4 + \gamma_4) P_{ik}^{n+1} = \frac{1}{\Delta t} P_{ik}^{n+\frac{1}{2}}, \text{for } k = N_z, \tag{A24}$$

where the homogeneous Neumann boundary condition is applied at $k=1$ and $k=N_z$. By using Equations (A20)–(A24), we can derive the following matrix form,

$$B_2 \mathbf{P}_i^{n+1} = \mathbf{P}_i^{n+\frac{1}{2}},$$

where B_2 is an $N_z \times N_z$ matrix,

$$B_2 = \begin{pmatrix} \alpha_4+\beta_4 & \gamma_4 & 0 & \cdots & 0 & 0 & 0 \\ \alpha_4 & \beta_4 & \gamma_4 & 0 & \cdots & 0 & 0 \\ 0 & \alpha_4 & \beta_4 & \gamma_4 & \cdots & 0 & 0 \\ 0 & 0 & \alpha_4 & \beta_4 & \gamma_4 & \cdots & 0 \\ \vdots & \vdots & \ddots & \ddots & \ddots & \vdots & \vdots \\ 0 & 0 & \cdots & 0 & \alpha_4 & \beta_4 & \gamma_4 \\ 0 & 0 & 0 & \cdots & 0 & \alpha_4 & \beta_4+\gamma_4 \end{pmatrix},$$

and

$$\mathbf{P}_i^{n+1} = \left(P_{i1}^{n+1}, \cdots, P_{iN_z}^{n+1}\right)^T, \text{and } \mathbf{P}_i^{n+\frac{1}{2}} = \left(P_{i1}^{n+\frac{1}{2}}, \cdots, P_{iN_z}^{n+\frac{1}{2}}\right)^T, \tag{A25}$$

for $i = b+1, b+2, ..., N_r$.